IOPscience iopscience.iop.org

Home Search Collections Journals About Contact us My IOPscience

Quantum noise of non-ideal Sagnac speed meter interferometer with asymmetries

This content has been downloaded from IOPscience. Please scroll down to see the full text.

2015 New J. Phys. 17 043031

(http://iopscience.iop.org/1367-2630/17/4/043031)

View the table of contents for this issue, or go to the journal homepage for more

Download details:

IP Address: 130.209.115.55
This content was downloaded on 19/01/2017 at 08:30

Please note that terms and conditions apply.

You may also be interested in:

Design of a speed meter interferometer proof-of-principle experiment
C Gräf, B W Barr, A S Bell et al.

Quantum limits of interferometer topologies for gravitational radiation detection
Haixing Miao, Huan Yang, Rana X Adhikari et al.

Candidates for a possible third-generation gravitational wave detector: comparison of ring-Sagnac and sloshing-Sagnac speedmeter interferometers
S H Huttner, S L Danilishin, B W Barr et al.

Advanced LIGO: length sensing and control in a dual recycled interferometric gravitational wave antenna
Kiwamu Izumi and Daniel Sigg

Squeezed light for the interferometric detection of high-frequency gravitational waves
R Schnabel, J Harms, K A Strain et al.

Advanced techniques in GEO 600
C Affeldt, K Danzmann, K L Dooley et al.

Quantum squeezed light in gravitational-wave detectors
S S Y Chua, B J J Slagmolen, D A Shaddock et al.

Achieving resonance in the advanced LIGO gravitational-wave interferometer
A Staley, D Martynov, R Abbott et al.

New Journal of Physics
The open access journal at the forefront of physics

Deutsche Physikalische Gesellschaft DPG
IOP Institute of Physics

Published in partnership with: Deutsche Physikalische Gesellschaft and the Institute of Physics

OPEN ACCESS

RECEIVED
9 December 2014

REVISED
19 February 2015

ACCEPTED FOR PUBLICATION
13 March 2015

PUBLISHED
16 April 2015

Content from this work may be used under the terms of the Creative Commons Attribution 3.0 licence.

Any further distribution of this work must maintain attribution to the author(s) and the title of the work, journal citation and DOI.

PAPER

Quantum noise of non-ideal Sagnac speed meter interferometer with asymmetries

S L Danilishin[1], C Gräf[2], S S Leavey[2], J Hennig[2], E A Houston[2], D Pascucci[2], S Steinlechner[2], J Wright[2] and S Hild[2]

[1] School of Physics, University of Western Australia, 35 Stirling Hwy, Crawley 6009, Australia
[2] SUPA, School of Physics and Astronomy, The University of Glasgow, Glasgow, G12 8QQ, UK

E-mail: Stefan.Danilishin@ligo.org

Keywords: gravitational wave detection, Sagnac speed meter, quantum noise suppression

Abstract

The speed meter concept has been identified as a technique that can potentially provide laser-interferometric measurements at a sensitivity level which surpasses the standard quantum limit (SQL) over a broad frequency range. As with other sub-SQL measurement techniques, losses play a central role in speed meter interferometers and they ultimately determine the quantum noise limited sensitivity that can be achieved. So far in the literature, the quantum noise limited sensitivity has only been derived for lossless or lossy cases using certain approximations (for instance that the arm cavity round trip loss is small compared to the arm cavity mirror transmission). In this article we present a generalized, analytical treatment of losses in speed meters that allows accurate calculation of the quantum noise limited sensitivity of Sagnac speed meters with arm cavities. In addition, our analysis allows us to take into account potential imperfections in the interferometer such as an asymmetric beam splitter or differences of the reflectivities of the two arm cavity input mirrors. Finally, we use the examples of the proof-of-concept Sagnac speed meter currently under construction in Glasgow and a potential implementation of a Sagnac speed meter in the Einstein Telescope to illustrate how our findings affect Sagnac speed meters with metre- and kilometre-long baselines.

1. Introduction

The sensitivity of state-of-the-art laser-interferometric gravitational wave detectors, such as the Advanced LIGO detector [1] currently being commissioned, will be limited over most frequencies in its detection band by so-called *quantum noise*. Quantum noise comprises of two components: sensing noise (photon shot noise) at high frequencies and back-action noise (photon radiation pressure noise) at low frequencies. One strategy for significant quantum noise reduction is to replace conventional position meters in these interferometers with a speed meter [2]. This allows, at least partially, the evasion of back-action noise and therefore provides the possibility of broadband sub-standard quantum limit (SQL) measurements [3].

The first implementation of a laser-interferometric speed meter was based on a Michelson interferometer employing an additional sloshing cavity in its output port [4–6]. In 2003, it was then shown by Chen that a Sagnac interferometer has inherent speed meter characteristics [7]. This article also included the first analytical treatment of the achievable suppression of back-action noise in a Sagnac speed meter, but did not include treatment of any effects arising from optical losses. Although the loss analysis in Michelson-based sloshing speed meters was done in [6], the first treatment of loss for a Sagnac speed meter was undertaken by Danilishin [8]. In the same article a new concept for a realization of a Sagnac speed meter based on polarization optics was suggested.

In the context of the Einstein Telescope (ET) design [9, 10], the analytical analysis of losses in speed meter interferometers was extended to Sagnac interferometers employing arm cavities as well as recycling techniques [11] and it was shown using theoretical analyses that speed meter interferometers can significantly outperform

© 2015 IOP Publishing Ltd and Deutsche Physikalische Gesellschaft

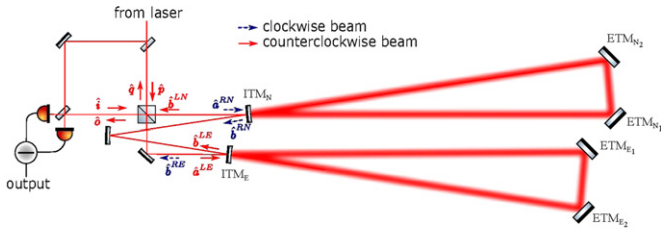

Figure 1. Simplified optical layout of a proof-of-concept speed meter interferometer with ring arm cavities that is being built in the University of Glasgow and that we will base our treatment of quantum noise on. Counterclockwise and clockwise beams as well as corresponding vacuum fields are denoted by blue (dashed) and red arrows, respectively.

traditional Michelson interferometers in terms of quantum noise [12, 13]. Additional work has shown that it is possible to implement a dc-readout technique [14, 15] based on polarization Sagnac interferometers [16]. Recently, the potential benefit of Sagnac speed meters for Advanced LIGO upgrades has been analysed and has also shown to be significant [17, 18].

While there has been significant effort over the past ten years to study aspects of speed meter configurations from a theoretical point of view, so far the performance of the speed meter concept has not been demonstrated in an experiment. Therefore, we recently started to set up a Sagnac speed meter proof-of-concept experiment, that aims to demonstrate the reduction of back-action noise provided by the speed meter [19].

In this article we further advance the quantum noise models for Sagnac speed meters, firstly by including treatment for asymmetries in the interferometer (such as an asymmetric beam splitter (BS) or arm cavity input-coupling mirrors with different reflectivities), and secondly by providing a more general treatment of losses. Furthermore, the losses do not rely on certain approximations, such as that arm cavity losses are much smaller than the input mirror transmission, an approximation made by all previous models.

In section 2 we lay out the theoretical background, framework and the details of our novel quantum noise model. We illustrate in section 3 the effects of interferometer asymmetries using two examples of vastly different arm lengths, from the metre-scale Glasgow Sagnac speed meter proof-of-concept experiment to the potential speed meter implementation for the 10 km long ET on the other hand. We conclude with a summary and outlook in section 4.

2. Analytical analysis of quantum noise in an imperfect and asymmetric Sagnac speed meter

In this section, we calculate quantum noise limited sensitivity (or more accurately its spectral density) for an imbalanced Sagnac interferometer featuring arm cavities, as shown in figure 1. This layout is chosen for a reason that it replicates the main design features of a proof-of-concept speed meter interferometer under construction at the University of Glasgow [19]. The most profound deviation of this setup from a large scale GW interferometer is that it has parallel arms, while the latter has orthogonal ones. However, we keep denoting the arms and all pertaining elements with the same letters N and E (meaning 'north'- and 'east'-bound arms, respectively) for compatibility with the earlier works [3, 7, 8].

The main purpose of this section is to show what impact different imperfections have on the realistic Sagnac speed meter's ability to suppress quantum back-action noise if compared to Michelson interferometers. In particular, we study how the deviation of the BS ratio from the ideal 50%/50% changes quantum noise. As well, the effect of non-identical arm cavities is considered. We study also the effect of optical loss in the elements of the core optics.

Consider first the underlying principle that makes Sagnac interferometer a speed meter. Indeed, visiting consequently both arms (see blue (dashed) and red arrows in figure 1), two counter propagating light beams are reflected sequentially from both arm cavities thereby acquiring phase shifts proportional to the sum of arms length variations $\Delta x_{N,E}(t) \equiv (x^{N,E}_{\rm ETM}(t) - x^{N,E}_{\rm ITM}(t))$ (hereinafter I(E)TM stands for input (end) test mass) of each of the cavities taken with time delay equal to average single cavity storage time $\tau_{\rm arm}$:

$$\delta\phi_R \propto \Delta x_N(t) + \Delta x_E\left(t + \tau_{\rm arm}\right), \tag{1}$$

$$\delta\phi_L \propto \Delta x_E(t) + \Delta x_N\left(t + \tau_{\rm arm}\right). \tag{2}$$

After recombining at the beamsplitter and photo detection the output signal turns out to be proportional to the phase difference of the clockwise (R) and the counter clockwise (L) propagating light beams:

$$\delta\phi_R - \delta\phi_L \propto \left[\Delta x_N(t) - \Delta x_N\left(t+\tau_{\rm arm}\right)\right] - \left[\Delta x_E(t) - \Delta x_E\left(t+\tau_{\rm arm}\right)\right]$$
$$\propto \Delta\dot{x}_N(t) - \Delta\dot{x}_E(t) + O(\tau_{\rm arm}) \quad (3)$$

that, for frequencies $\ll\tau_{\rm arm}^{-1}$, is proportional to relative rate of the interferometer arms length variation, i.e. their relative speed.

Note also that the optical paths of the two beams are absolutely identical irrespective of the difference in length of the two arms, if looked at on a time scale longer than $\tau_{\rm arm}$. Therefore, a Sagnac interferometer naturally keeps its output port dark at dc frequencies. It is only the dynamical change of the arms lengths faster than $\tau_{\rm arm}$ that leads to a non-zero signal at the output photodetector.

We start the analysis of the scheme with choosing the proper notations for the optical fields on key elements of the interferometer. Unlike in Michelson interferometer, in Sagnac interferometers all photons pass through both arm cavities before recombining with a counter-propagating beam at the BS. At the same time, the two light beams hit the cavity simultaneously, one coming directly from the BS and the other one, that has just left the other arm. In notations of Chen's paper [7], quadrature operators of light entering and leaving the arm can be marked with two indices IJ, e.g. a_c^{IJ}, where I stands for the either of two beams, L or R, and J stands for the either of two arms ($J = E,\ N$). Here R marks the light beam that first enters North arm and then travels the interferometer in the right direction (clockwise), and L marks the beam travelling the interferometer in the opposite (counterclockwise) direction after entering the interferometer through the East arm.

2.1. Two-photon formalism for quantized light

Quantum noise in interferometers originates from the quantum nature of light [20]. We will use the so called *two-photon formalism* of Caves and Schumaker [21, 22] to describe quantized light and its quantum fluctuations in the most convenient manner for optomechanical displacement sensors, of which GW interferometers, including the Sagnac speed meter, make an important class.

The monochromatic electromagnetic wave with a central frequency $\omega_0 = 2\pi c/\lambda_0$ and λ_0 its wavelength, can be characterized by its electric field strain. At an arbitrary point of space, characterized by the coordinate vector $\mathbf{r} = \{x,\ y,\ z\}$, its space-time dependence can be written as:

$$\hat{E}(\mathbf{r},\ t) = \mathcal{E}_0 u(\mathbf{r})\left[\left(A_c + \hat{a}_c(t)\right)\cos\omega_0 t + \left(A_s + \hat{a}_s(t)\right)\sin\omega_0 t\right], \quad (4)$$

where $\mathcal{E}_0 = \sqrt{4\pi\hbar\omega_0/(\mathcal{A}c)}$ with $\mathcal{A}$ the cross-section area of the light beam. Factor $u(\mathbf{r})$ describes the spatial structure of the light field that may be quite peculiar. For our analysis, this factor is irrelevant as it does not influence quantum noise spectrum. Here we separated *sine* and *cosine* quadrature amplitudes in a classical (denoted by capital letters, $A_{c,s}$) and quantum fluctuation (small capped letters, $\hat{a}_{c,s}(t)$) parts, to track their propagation through the interferometer separately. Hence, the dynamics of the light field in the interferometer is reduced to the transformation of the two-dimensional quadrature vectors:

$$\mathbf{A} = \begin{bmatrix} A_c \\ A_s \end{bmatrix}, \quad \text{and} \quad \hat{\mathbf{a}} = \begin{bmatrix} \hat{a}_c \\ \hat{a}_s \end{bmatrix}. \quad (5)$$

Usually, the analysis of light in linear optical devices is performed in Fourier domain. For the noise quadrature amplitudes it is done straightforwardly using the Fourier transform:

$$\hat{a}_{c,s}(t) = \int_{-\infty}^{\infty} \frac{\mathrm{d}\Omega}{2\pi}\hat{a}_{c,s}(\Omega)\,\mathrm{e}^{-\mathrm{i}\Omega t}, \quad (6)$$

where $\Omega = \omega - \omega_0$ stands for the offset from the carrier frequency ω_0. In the following we will use only the Fourier picture and omit the argument Ω for convenience and clearer presentation.

2.2. Input–output relations for a linear optomechanical device

An optomechanical device can be characterized by a transformation that the mechanical motion of its parts imprints on the light passing through, or reflected from it. A Sagnac interferometer is a clear example of the optomechanical sensor. To calculate its quantum noise we need to find how the input fluctuations of the light, characterized by quadrature amplitudes $\hat{\mathbf{a}}^{\rm in} = \{\hat{a}_c^{\rm in},\ \hat{a}_s^{\rm in}\}^{\rm T}$, get transformed by the interferometer into the output quadratures, $\hat{\mathbf{b}}^{\rm out} = \{\hat{b}_c^{\rm out},\ \hat{b}_s^{\rm out}\}^{\rm T}$. This task can be conveniently solved using a transfer matrix, or input–output (I/O) relations approach in the Fourier domain that can be written in general form as:

$$\hat{\mathbf{b}}^{\rm out} = \mathbb{T}\cdot\hat{\mathbf{a}}^{\rm in} + \mathbf{R}_x x/x_{\rm SQL}, \quad (7)$$

where

$$\mathbb{T} \equiv \begin{bmatrix} T_{cc}(\Omega) & T_{cs}(\Omega) \\ T_{sc}(\Omega) & T_{ss}(\Omega) \end{bmatrix} \tag{8}$$

is the optical transfer matrix of the interferometer

$$\mathbf{R}_x \equiv \begin{bmatrix} R_{x,c}(\Omega) \\ R_{x,s}(\Omega) \end{bmatrix} \tag{9}$$

is an optical response of the interferometer on a mirror displacement with spectrum $x(\Omega)$, and

$$x_{\mathrm{SQL}} = \sqrt{\frac{2\hbar}{M\Omega^2}} \tag{10}$$

is the free-mass amplitude spectral density (ASD) of the SQL in terms of mirror displacement for an interferometer with the effective mechanical displacement mode mass M.

The output signal of the interferometer is usually contained in a photocurrent of a photodetector, or, if a more advanced readout technique is used, the difference current of a balanced homodyne detector, $\hat{i}_\zeta^{\,\mathrm{out}}$ that is proportional to the output light quadrature with the homodyne angle ζ:

$$\hat{i}_\zeta^{\,\mathrm{out}} \propto \hat{b}_c^{\,\mathrm{out}} \cos\zeta + \hat{b}_s^{\,\mathrm{out}} \sin\zeta \equiv \mathbf{H}_\zeta^{\mathrm{T}} \cdot \hat{\boldsymbol{b}}, \quad \mathbf{H}_\zeta \equiv \begin{bmatrix} \cos\zeta \\ \sin\zeta \end{bmatrix}. \tag{11}$$

The corresponding quantum noise spectral density in the desired units, e.g. in units of displacement, can be obtained from the above using the following simple rule:

$$S^{x}(\Omega) = x_{\mathrm{SQL}}^2 \frac{\mathbf{H}_\zeta^{\mathrm{T}} \cdot \mathbb{T} \cdot \mathbb{S}_a^{\mathrm{in}} \cdot \mathbb{T}^\dagger \cdot \mathbf{H}_\zeta}{\left|\mathbf{H}_\zeta^{\mathrm{T}} \cdot \mathbf{R}_x\right|^2}, \tag{12}$$

where $\mathbb{S}_a^{\mathrm{in}}$ is the spectral density matrix of the incident light, whose components are defined as:

$$2\pi\delta(\Omega - \Omega')\mathbb{S}_{a,ij}^{\mathrm{in}}(\Omega) \equiv \frac{1}{2}\langle \mathrm{in}|\, \hat{a}_i^{\mathrm{in}}(\Omega)\left(\hat{a}_j^{\mathrm{in}}(\Omega')\right)^\dagger + \left(\hat{a}_j^{\mathrm{in}}(\Omega')\right)^\dagger \hat{a}_i^{\mathrm{in}}(\Omega)\,|\mathrm{in}\rangle, \tag{13}$$

where $|\mathrm{in}\rangle$ is the quantum state of the light injected into the dark port of the interferometer and $(i, j) = (c, s)$ (see section 3.3 in [3] for more details).

2.3. Quantum noise in a real lossy interferometer

The procedure described above is idealized because it neither takes into account optical losses and the associated additional quantum noise, nor the asymmetry present in any real balanced scheme. In order to take those factors into account it is necessary to (i) consider arms of the interferometer separately and (ii) take into account optical loss in all elements of the scheme and add the corresponding incoherent noise terms into the inputs of the interferometer input–output (I/O) relations.

This leads to an expansion of the number of inputs of the interferometer for, e.g., in a lossy system for each particular loss point one has to introduce a corresponding vacuum noise field according to the fluctuation–dissipation theorem [23]. So, if one has a system with N input fields, $\hat{\boldsymbol{a}}_j^{\mathrm{in}}$, and M loss-associated noise fields, $\hat{\boldsymbol{n}}_k$, the corresponding expression for the quantum noise spectral density will be just a trivial sum of spectral densities of the individual noise sources:

$$S^{x}(\Omega) = x_{\mathrm{SQL}}^2 \frac{\sum_{j=1}^{N} \mathbf{H}_\zeta^{\mathrm{T}} \cdot \mathbb{T}_j \cdot \mathbb{S}_{a_j}^{\mathrm{in}} \cdot \mathbb{T}_j^\dagger \cdot \mathbf{H}_\zeta + \sum_{k=1}^{M} \mathbf{H}_\zeta^{\mathrm{T}} \cdot \mathbb{N}_k \cdot \mathbb{N}_k^\dagger \cdot \mathbf{H}_\zeta}{\left|\mathbf{H}_\zeta^{\mathrm{T}} \cdot \mathbf{R}_x\right|^2}, \tag{14}$$

where $\mathbb{S}_{a_j}^{\mathrm{in}}$ are (single-sided) spectral density matrices for all independent inputs, and we accounted for the special shape of a vacuum state spectral density matrix of the loss-associated vacuum fields, $\mathbb{S}_{n_k}^{\mathrm{in}} = \mathbb{I}$—identity matrix (see, e.g. section 3.2.1 of [3]).

2.4. Input–output relations for a symmetric lossless Sagnac interferometer

Before doing a full analysis of a lossy imperfect Sagnac interferometer, let us recall briefly the derivation of I/O-relations for a lossless Sagnac interferometer as is done in Chen's paper [7] and keeping to his notations as described above:

$$b_c^{IJ} = \mathrm{e}^{2\mathrm{i}\beta_{\mathrm{arm}}(\Omega)} a_c^{IJ}, \tag{15}$$

$$b_s^{IJ} = e^{2i\beta_{\mathrm{arm}}(\Omega)}\left[a_s^{IJ} - \mathcal{K}_{\mathrm{arm}}^{IJ} a_c^{IJ} - \mathcal{K}_{\mathrm{arm}}^{\bar{I}J} a_c^{\bar{I}J}\right] + \mathrm{e}^{\mathrm{i}\beta_{\mathrm{arm}}(\Omega)}\sqrt{2\mathcal{K}_{\mathrm{arm}}^{IJ}}\frac{\sqrt{2}x_J}{x_{\mathrm{SQL}}} \tag{16}$$

with $\bar{I}$ indicating the beam propagating in opposite direction with respect to I, i.e. $\bar{R} = L$ and $\bar{L} = R$, and $x_J = x_J^{\mathrm{ETM}} - x_J^{\mathrm{ITM}}$ is the signal-induced arm elongation[3]. Here we introduce the optomechanical coupling coefficients, $\mathcal{K}_{\mathrm{arm}}^{IJ}$, for each beam separately. This notation helps us later on to account for asymmetries in the interferometer. For the definition of $\mathcal{K}_{\mathrm{arm}}^{IJ}$ we follow the Kimble *et al* paper [24]:

$$\mathcal{K}_{\mathrm{arm}}^{IJ} = \frac{2\Theta^{IJ}\gamma_{\mathrm{arm}}}{\Omega^2\left(\gamma_{\mathrm{arm}}^2 + \Omega^2\right)}, \quad \text{with} \quad \Theta^{IJ} = \frac{4\omega_0 P_c^{IJ}}{\mu_{\mathrm{arm}} cL}, \tag{17}$$

$$\beta_{\mathrm{arm}} = \arctan\frac{\Omega}{\gamma_{\mathrm{arm}}}, \tag{18}$$

where $\gamma_{\mathrm{arm}} = cT_{\mathrm{ITM}}/(4L)$ is the arm cavity half-banwidth, P_c^{IJ} stands for optical power circulating in the arm in one direction, i.e. in the R-beam, or in the L-beam, and $\mu_{\mathrm{arm}} = 2M_{\mathrm{ITM}}M_{\mathrm{ETM}}/(M_{\mathrm{ITM}} + 2M_{\mathrm{ETM}})$ is the effective mass of the arm.

Now it is straightforward to derive full I/O-relations for a lossless symmetric Sagnac interferometer. In this case, the optomechanical coupling coefficients are the same for all beams, i.e. $\mathcal{K}_{\mathrm{arm}}^{IJ} \equiv \mathcal{K}_{\mathrm{arm}}$. Then, using junction equations for the fields at the BS:

$$\hat{\boldsymbol{a}}^{RN} = \frac{\hat{\boldsymbol{p}} + \hat{\boldsymbol{i}}}{\sqrt{2}}, \quad \hat{\boldsymbol{a}}^{LE} = \frac{\hat{\boldsymbol{p}} - \hat{\boldsymbol{i}}}{\sqrt{2}}, \quad \hat{\boldsymbol{o}} = \frac{\hat{\boldsymbol{b}}^{LN} - \hat{\boldsymbol{b}}^{RE}}{\sqrt{2}}, \tag{19}$$

as well as continuity relations between the beams that leave one arm and enter the other:

$$\hat{\boldsymbol{a}}^{RE} = \hat{\boldsymbol{b}}^{RN}, \quad \hat{\boldsymbol{a}}^{LN} = \hat{\boldsymbol{b}}^{LE}, \tag{20}$$

one obtains:

$$\begin{bmatrix}\hat{o}_c\\ \hat{o}_s\end{bmatrix} = \mathrm{e}^{2\mathrm{i}\beta_{\mathrm{sag}}}\begin{bmatrix}1 & 0\\ -\mathcal{K}_{\mathrm{sag}} & 1\end{bmatrix}\begin{bmatrix}\hat{i}_c\\ \hat{i}_s\end{bmatrix} + \begin{bmatrix}0\\ \sqrt{2\mathcal{K}_{\mathrm{sag}}}\end{bmatrix}\mathrm{e}^{\mathrm{i}\beta_{\mathrm{sag}}}\frac{x_-}{x_{\mathrm{SQL}}}, \tag{21}$$

with the coupling constant $\mathcal{K}_{\mathrm{sag}}$ defined as:

$$\mathcal{K}_{\mathrm{sag}} = 8\mathcal{K}_{\mathrm{arm}}\sin^2\beta_{\mathrm{arm}} = \frac{4\Theta\gamma_{\mathrm{arm}}}{\left(\Omega^2 + \gamma_{\mathrm{arm}}^2\right)^2}, \tag{22}$$

and phase shift:

$$\beta_{\mathrm{sag}} = 2\beta_{\mathrm{arm}} + \frac{\pi}{2}. \tag{23}$$

Here we define the differential mechanical mode of the interferometer as $x_- = x_N - x_E$ (the common mode is defined by analogy as $x_+ = x_N + x_E$).

The noise transfer matrix and signal response vector for this case have a particularly concise form:

$$\mathbb{T} = -\mathrm{e}^{2\mathrm{i}\beta_{\mathrm{sag}}}\begin{bmatrix}1 & 0\\ -\mathcal{K}_{\mathrm{sag}} & 1\end{bmatrix}, \quad \mathbf{R} = \mathrm{e}^{\mathrm{i}\beta_{\mathrm{sag}}}\begin{bmatrix}0\\ \sqrt{2\mathcal{K}_{\mathrm{sag}}}\end{bmatrix}. \tag{24}$$

Therefore one gets the following simple expression for the spectral density of the quantum noise limited sensitivity of the zero-area Sagnac interferometer (it is the same for all tuned interferometers with a balanced homodyne readout of quadrature b_ζ and a vacuum state at the dark port, save to the expression for $\mathcal{K}$) :

$$S^{x_-} = \frac{x_{\mathrm{SQL}}^2}{2}\left\{\frac{\left[\mathcal{K}_{\mathrm{sag}} - \cot\zeta\right]^2 + 1}{\mathcal{K}_{\mathrm{sag}}}\right\}. \tag{25}$$

[3] Note that the factor $\sqrt{2}$ in front of the arm mechanical mode coordinate x_J in equation (16) is due to the difference between the effective mass of the arm, μ_{arm}, and that of the whole interferometer $M = \mu_{\mathrm{arm}}/2$, that enters the expression for x_{SQL} in equation (10).

2.5. Asymmetric BS

The main asymmetry one can think of in a Sagnac interferometer is the non-perfect splitting ratio of the main BS resulting in an imbalance of the power in the two light beams propagating in opposite directions. As our analysis demonstrates below, this imbalance leads to a dramatic increase of the residual radiation pressure noise, amounting to a steeper rise of the quantum noise towards lower frequencies, $S_x^{\mathrm{r.p.}} \propto f^{-6}$, than that of a Michelson interferometer.

In order to account for this asymmetry in our quantum noise calculations let us define the BS symmetry offset, η_{BS}, through the BS power reflectivity, R_{BS}, and transmissivity, T_{BS}, as:

$$\sqrt{R_{\mathrm{BS}}} = \frac{1+\eta_{\mathrm{BS}}}{\sqrt{2}}, \quad \sqrt{T_{\mathrm{BS}}} = \frac{1-\eta_{\mathrm{BS}}}{\sqrt{2}}. \tag{26}$$

Then the Sagnac I/O-relations with an asymmetric BS read (see figure 3 for field operator notations):

$$\hat{\boldsymbol{o}} = \frac{\hat{\boldsymbol{b}}^{LN} - \hat{\boldsymbol{b}}^{RE}}{\sqrt{2}} + \eta_{\mathrm{BS}}\frac{\hat{\boldsymbol{b}}^{LN} + \hat{\boldsymbol{b}}^{RE}}{\sqrt{2}}, \quad \hat{\boldsymbol{q}} = \frac{\hat{\boldsymbol{b}}^{LN} + \hat{\boldsymbol{b}}^{RE}}{\sqrt{2}} - \eta_{\mathrm{BS}}\frac{\hat{\boldsymbol{b}}^{LN} - \hat{\boldsymbol{b}}^{RE}}{\sqrt{2}},$$
$$\hat{\boldsymbol{a}}^{RN} = \frac{\hat{\boldsymbol{p}} + \hat{\boldsymbol{i}}}{\sqrt{2}} + \eta_{\mathrm{BS}}\frac{\hat{\boldsymbol{p}} - \hat{\boldsymbol{i}}}{\sqrt{2}}, \quad \hat{\boldsymbol{a}}^{LE} = \frac{\hat{\boldsymbol{p}} - \hat{\boldsymbol{i}}}{\sqrt{2}} - \eta_{\mathrm{BS}}\frac{\hat{\boldsymbol{p}} + \hat{\boldsymbol{i}}}{\sqrt{2}},$$

Using these expressions one can immediately see that the classical amplitudes of the two beams, leaving the BS, are uneven, i.e. $A^{RN} = P(1+\eta_{\mathrm{BS}})/\sqrt{2}$ and $A^{LE} = P(1-\eta_{\mathrm{BS}})/\sqrt{2}$ (P is a classical amplitude of pump field , $\hat{\boldsymbol{p}}$, and we assume no classical component for the field entering through the dark port, $I=0$). Therefore, the same is true for the intracavity fields and thereby for the optomechanical coupling factors $\mathcal{K}_{\mathrm{arm}}^{IJ}$, which can now be written as:

$$\mathcal{K}_{\mathrm{arm}}^{RN} = \mathcal{K}_{\mathrm{arm}}^{RE} = \mathcal{K}_{\mathrm{arm}}\left(1+\eta_{\mathrm{BS}}\right)^2, \quad \mathcal{K}_{\mathrm{arm}}^{LE} = \mathcal{K}_{\mathrm{arm}}^{LN} = \mathcal{K}_{\mathrm{arm}}\left(1-\eta_{\mathrm{BS}}\right)^2, \tag{27}$$

which indicates the imbalance in the radiation pressure force responsible for the effect we are describing in this subsection.

The I/O-relations for the Sagnac interferometer with an asymmetric BS can be written as:

$$\hat{\boldsymbol{o}} = \mathbb{T}_i^{\mathrm{asym.BS}}\hat{\boldsymbol{i}} + \mathbb{T}_p^{\mathrm{asym.BS}}\hat{\boldsymbol{p}} + \mathbf{R}_- x_- / x_{\mathrm{SQL}} + \mathbf{R}_+ x_+ / x_{\mathrm{SQL}}, \tag{28}$$

where the quantum noise transfer matrices read:

$$\mathbb{T}_i^{\mathrm{asym.BS}} = \left(1-\eta_{\mathrm{BS}}^2\right)\mathrm{e}^{2i\beta_{\mathrm{sag}}}\begin{bmatrix} 1 & 0 \\ -\left[\mathcal{K}_{\mathrm{sym}}^{\mathrm{sag}} + \eta_{\mathrm{BS}}^2\mathcal{K}_{\mathrm{asym}}^{\mathrm{sag}}\right] & 1 \end{bmatrix},$$
$$\mathbb{T}_p^{\mathrm{asym.BS}} = 2\eta_{\mathrm{BS}}\mathrm{e}^{2i\beta_{\mathrm{sag}}}\begin{bmatrix} 1 & 0 \\ -\frac{1}{2}\left[\left(1+3\eta_{\mathrm{BS}}^2\right)\mathcal{K}_{\mathrm{sym}}^{\mathrm{sag}} + \left(3+\eta_{\mathrm{BS}}^2\right)\mathcal{K}_{\mathrm{asym}}^{\mathrm{sag}}\right] & 1 \end{bmatrix}$$

and where we define the new phase shift, β_{sag}, and the symmetric and asymmetric components of the optomechanical coupling as:

$$\mathcal{K}_{\mathrm{sym}}^{\mathrm{sag}} = 4\mathcal{K}_{\mathrm{arm}}\sin^2\beta_{\mathrm{arm}} = \frac{8\Theta\gamma_{\mathrm{arm}}}{\left(\gamma_{\mathrm{arm}}^2+\Omega^2\right)^2}, \tag{29}$$

$$\mathcal{K}_{\mathrm{asym}}^{\mathrm{sag}} = 4\mathcal{K}_{\mathrm{arm}}\cos^2\beta_{\mathrm{arm}} = \frac{8\Theta\gamma_{\mathrm{arm}}^3}{\Omega^2\left(\gamma_{\mathrm{arm}}^2+\Omega^2\right)^2}, \tag{30}$$

and $\beta_{\mathrm{sag}} = 2\beta_{\mathrm{arm}} + \pi/2$.

Quite expectedly, an asymmetry of the BS results in the common mode (x_+), signal showing up at the output port on a par with the differential mode. The two response functions for the cARM and the dARM signal read:

$$\mathbf{R}_- = \mathrm{e}^{i\beta_{\mathrm{sag}}}\left(1+\eta_{\mathrm{BS}}^2\right)\sqrt{2\mathcal{K}_{\mathrm{sym}}^{\mathrm{sag}}}\begin{bmatrix}0\\1\end{bmatrix},$$
$$\mathbf{R}_+ = 2\eta_{\mathrm{BS}}\mathrm{e}^{2i\beta_{\mathrm{arm}}}\sqrt{2\mathcal{K}_{\mathrm{asym}}^{\mathrm{sag}}}\begin{bmatrix}0\\1\end{bmatrix}. \tag{31}$$

It is now straightforward to the calculate spectral density of quantum noise in units of dARM displacement, using equation (12):

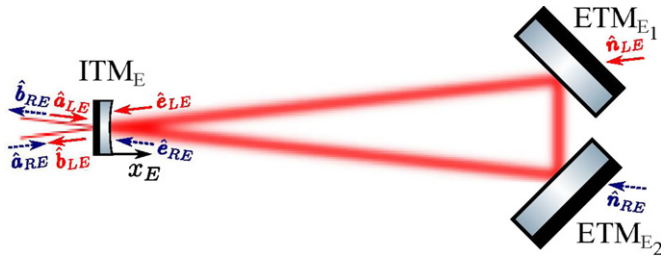

Figure 2. Schematic of a Sagnac ring arm cavity with marked input and output fields. The 'east' arm cavity is chosen for definiteness.

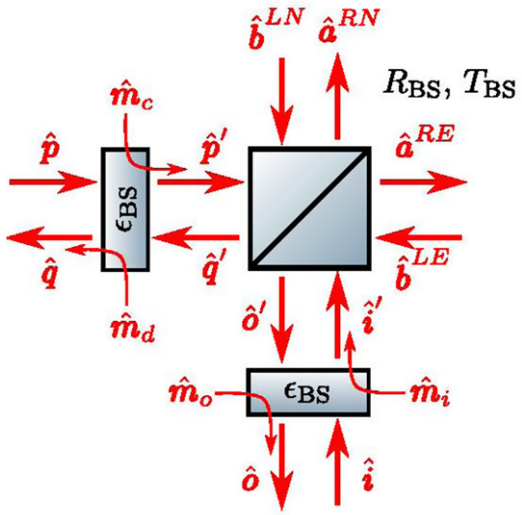

Figure 3. Schematic of a lossy beamsplitter and its I/O-relations and fields.

$$S^{x_-}_{\text{asym. BS}} = \frac{x^2_{\text{SQL}}}{2\mathcal{K}^{\text{sag}}_{\text{sym}}}\left\{\left(\frac{1-\eta^2_{\text{BS}}}{1+\eta^2_{\text{BS}}}\right)^2\left(1+\left[\mathcal{K}^{\text{sag}}_{\text{sym}}+\eta^2_{\text{BS}}\mathcal{K}^{\text{sag}}_{\text{asym}}-\cot\zeta\right]^2\right)\right.$$
$$\left.+\left(\frac{2\eta_{\text{BS}}}{1+\eta^2_{\text{BS}}}\right)^2\left(1+\left[\frac{1}{2}\left[\left(1+3\eta^2_{\text{BS}}\right)\mathcal{K}^{\text{sag}}_{\text{sym}}+\left(3+\eta^2_{\text{BS}}\right)\mathcal{K}^{\text{sag}}_{\text{asym}}\right]-\cot\zeta\right]^2\right)\right\}. \quad (32)$$

Despite relative complexity of this formula, the origin of predicted steep rise of the quantum noise at low frequencies can be easily seen through. It directly follows from behaviour of $\mathcal{K}^{\text{sag}}_{\text{asym}}$ and $\mathcal{K}^{\text{sag}}_{\text{sym}}$ at low frequencies $\Omega \ll \gamma_{\text{arm}}$. Since $\mathcal{K}^{\text{sag}}_{\text{sym}}(\Omega \to 0) \propto \text{const}$, $\mathcal{K}^{\text{sag}}_{\text{asym}}(\Omega \to 0) \propto \Omega^{-2}$ and $x^2_{\text{SQL}} \propto \Omega^{-2}$, the terms responsible for $\propto \Omega^{-6}$ rise are those proportional to $(\mathcal{K}^{\text{sag}}_{\text{ssym}})^2 \propto \Omega^{-4}$ inside the braces. Together with $x^2_{\text{SQL}} \propto \Omega^{-2}$ it gives the predicted behaviour.

2.6. Losses in the arm cavities

The next important source of imperfection in a Sagnac interferometer is optical loss in the arm cavities.

Each arm cavity of the Sagnac interferometer can be considered as a Fabry–Pérot-type ring cavity with movable mirrors as shown in figure 2 . To account for losses in the arms we have to introduce additional vacuum fields in accordance with the fluctuation–dissipation theorem [23]. For all practical purposes it is sufficient to model it by attributing an additional transmissivity to the end mirrors (ETMs), T_{loss}. In this case, the general structure of the I/O-relations will remain similar to equations (15) and (17), but with additional vacuum noise fields originating from loss:

$$\hat{\boldsymbol{b}}^{IJ} = \mathbb{T}^{IJ}_{\text{arm}}\cdot\hat{\boldsymbol{a}}^{IJ} + \mathbb{N}^{IJ}_{\text{arm}}\cdot\hat{\boldsymbol{n}}^{IJ} + \mathbb{T}^{\bar{I}J}_{\text{arm,r.p.}}\cdot\hat{\boldsymbol{a}}^{\bar{I}J} + \mathbb{N}^{\bar{I}J}_{\text{arm,r.p.}}\cdot\hat{\boldsymbol{n}}_{\bar{I}J} + \mathbf{R}^{IJ}_{\text{arm}}\frac{x_J}{x_{\text{SQL}}}, \quad (33)$$

where $\hat{\boldsymbol{a}}^{IJ}$ and $\mathbb{T}^{IJ}_{\rm arm}$ stand for for vacuum field entering the arm cavity through the ITM and its transfer matrix, $\mathbb{T}^{\tilde{I}J}_{\rm arm,r.p.}$, represents a part of the full transfer matrix resulting from radiation pressure created by the counter propagating light beam, $\hat{\boldsymbol{n}}^{IJ}$ and $\mathbb{N}^{IJ}_{\rm arm}$ stand for the loss-associated vacuum field entering the arm cavity through the ETM and its transfer matrix, $\mathbb{N}^{\tilde{I}J}_{\rm arm,r.p.}$ is the radiation pressure component of the latter, while $\mathbf{R}^{IJ}$ is the cavity response to the mirror displacement. Entry points of all participating vacuum fields are shown schematically in figure 2.

Optical loss in the Sagnac interferometer manifests itself in two ways that conspire to undermine the radiation pressure suppression effect of the speed meter. Firstly, the power of the light beam when it leaves the first arm cavity towards the second cavity is reduced by a factor $\epsilon_{\rm arm} = T_{\rm loss}/(T_{\rm ITM} + T_{\rm loss})$, and therefore the radiation pressure force it creates in the second cavity is less than that in the first one. As a result, the perfect subtraction of radiation pressure forces becomes impossible. Secondly, the additional uncorrelated vacuum noise that accompanies the light beam at its second reflection of the arm cavity, right before the recombination at the BS, creates an uncompensated radiation pressure force akin to that of a Michelson interferometer. These two effects together are responsible for the rise of the quantum noise at the low frequencies.

In order to distinguish the symmetric loss effect from the effect of imbalance, it is reasonable to represent the cavity mirror parameters as a sum of symmetric and anti-symmetric components in the following way:

$$T^{J}_{\rm ITM} = T_{\rm ITM} \pm \delta T_{\rm ITM}/2, \quad \Leftrightarrow \quad T_{\rm ITM} = \frac{T^{N}_{\rm ITM} + T^{E}_{\rm ITM}}{2}, \quad \delta T_{\rm ITM} = T^{N}_{\rm ITM} - T^{E}_{\rm ITM}.$$

$T^{J}_{\rm loss}$ can be represented in a similar way. Then one can represent all the arm-related imperfections in terms of four parameters, namely:

(i) average bandwidth, $\gamma_{\rm arm} = \dfrac{c\,(T_{\rm ITM} + T_{\rm loss})}{4L}$;

(ii) its imbalance $\delta\gamma = \dfrac{c\,(\delta T_{\rm ITM} + \delta T_{\rm loss})}{4L}$;

(iii) average fractional loss of photons per round trip per cavity, $\epsilon_{\rm arm} = \dfrac{T_{\rm loss}}{T_{\rm ITM} + T_{\rm loss}}$;

(iv) and associated imbalance $\delta\epsilon_{\rm arm} \simeq \dfrac{\delta T_{\rm loss}}{T_{\rm ITM} + T_{\rm loss}}$.

Another common feature of these imperfections, confirmed by numerical estimates based on general treatment outlined in appendix A is that their impact is noticeable only at frequencies well below the arm cavity bandwidth, i.e. for $\Omega \ll \gamma_{\rm arm}$. Keeping this in mind and using the introduced parameters, one can rewrite optomechanical coupling factors for the arms, defined in (17) as (we set $\eta_{\rm BS} = 0$ here for simplicity and to isolate the effect of the arms from that of the BS):

$$\mathcal{K}^{RN}_{\rm arm} = \mathcal{K}_{\rm arm}\left\{1 - \frac{\delta\gamma}{\gamma_{\rm arm}} - \frac{\delta\epsilon_{\rm arm}}{2} - \epsilon_{\rm arm}\left(1 - \frac{\delta\gamma}{\gamma_{\rm arm}}\right)\right\}, \tag{34a}$$

$$\mathcal{K}^{LE}_{\rm arm} = \mathcal{K}_{\rm arm}\left\{1 + \frac{\delta\gamma}{\gamma_{\rm arm}} + \frac{\delta\epsilon_{\rm arm}}{2} - \epsilon_{\rm arm}\left(1 + \frac{\delta\gamma}{\gamma_{\rm arm}}\right)\right\}, \tag{34b}$$

$$\mathcal{K}^{RE}_{\rm arm} = \mathcal{K}_{\rm arm}\left\{1 - \frac{\delta\gamma}{\gamma_{\rm arm}} - \epsilon_{\rm arm}\left(2 - \frac{\delta\gamma}{\gamma_{\rm arm}} + \frac{\delta\epsilon_{\rm arm}}{2}\right) + \epsilon^2_{\rm arm}\right\}, \tag{34c}$$

$$\mathcal{K}^{LN}_{\rm arm} = \mathcal{K}_{\rm arm}\left\{1 + \frac{\delta\gamma}{\gamma_{\rm arm}} - \epsilon_{\rm arm}\left(2 + \frac{\delta\gamma}{\gamma_{\rm arm}} - \frac{\delta\epsilon_{\rm arm}}{2}\right) + \epsilon^2_{\rm arm}\right\}. \tag{34d}$$

One can see that the effect of symmetric loss on the optomechanical interaction ($\delta\gamma = \delta\epsilon_{\rm arm} = 0$) is reduced to the multiplication of the loss-free $\mathcal{K}$ by $(1 - \epsilon_{\rm arm})$ in the first passage of the beam through the arm cavity (*RN* and *LE* beams), and by $(1 - \epsilon_{\rm arm})^2$ in the second passage (*RE* and *LN* beams), which is expectable. The phase shift $\beta_{\rm arm}$ is also modified by loss and asymmetry via $\gamma^{J}_{\rm arm} \to \gamma^{J}_{\rm arm}(1 + \epsilon_{\rm arm} \pm \delta\epsilon_{\rm arm}/2)$, but the increment is a second order correction $\sim\mathcal{O}\,(\epsilon_{\rm arm}\Omega/\gamma_{\rm arm})$ and therefore omitted.

Inserting these expressions into equations (A.19) for the transfer matrices of lossy arms and then into (A.20), one gets the I/O-relations for lossy arms of the form shown in equation (33). Using symmetric BS relations (refer to equations (19) and (20)), one can finally obtain the I/O-relations for a Sagnac interferometer with loss in the arms and get the expression for the spectral density, which is rather involved. However, the general structure of it

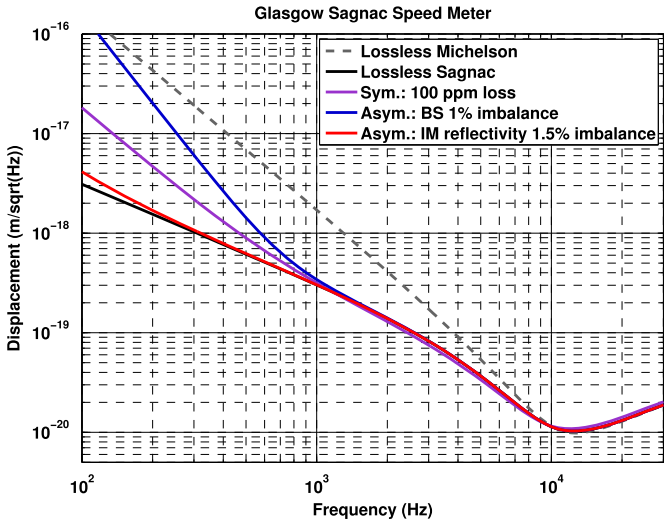

Figure 4. Spectral density plots for a table-top Sagnac interferometer with parameters given in table 1. Here we demonstrate what impact different imperfections have on the quantum noise sensitivity of the interferometer. All plots are drawn for phase quadrature readout, i.e. for homodyne angle $\zeta = \pi/2$. Ideal Michelson interferometer parameters match those of the corresponding ideal Sagnac interferometer, shown in the same plot.

can be represented as follows:

$$S^{x_-}_{\rm loss} = S^{x_-} + \frac{x^2_{\rm SQL}}{2}\mathcal{K}_{\rm arm}\Big\{L_{\rm sym}\left(\epsilon_{\rm arm},\, \epsilon^2_{\rm arm},\, \ldots\right) + L_{\rm asym}\left(\delta\epsilon^2_{\rm arm},\, \frac{\delta\gamma\delta\epsilon_{\rm arm}}{\gamma_{\rm arm}},\, \left(\frac{\delta\gamma}{\gamma_{\rm arm}}\right)^2\right) + \mathcal{O}\left(\delta\epsilon^3_{arm},\, \left(\delta\gamma/\gamma_{\rm arm}\right)^3,\, \ldots\right)\Big\}, \tag{35}$$

where S^{x_-} stands for the lossless Sagnac interferometer quantum noise spectral density of equation (25) and both, $L_{\rm sym}$ and $L_{\rm asym}$, are linear functions. As one can see, the influence of loss in general is dictated by the factor $\mathcal{K}_{\rm arm}$ in front of the bracket which rises as $1/\Omega^2$ at low frequencies and combined with $x^2_{\rm SQL} \propto 1/\Omega^2$ gives exactly the Michelson-like raise of quantum noise at low frequencies.

Asymmetries in the arms have a second-order influence, as indicated by the powers of the arguments of $L_{\rm asym}$. In contrast symmetric loss has a first-order contribution to the total quantum noise of a Sagnac interferometer. These trends are demonstrated in figure 4, and the detailed behaviour of quantum noise as a function of symmetric loss, $\epsilon_{\rm arm}$, is shown in figure 5 . The influence of asymmetry of the ITM transmissivities, or $\delta\gamma/\gamma_{\rm arm}$, is shown in figure 7. The asymmetric loss, $\delta\epsilon_{\rm arm}$, has a similarly weak impact.

2.7. General treatment of quantum noise of asymmetric Sagnac interferometer

For proper treatment of quantum noise in an asymmetric Sagnac, we need to specify the I/O-relations for a lossy BS with arbitrary splitting ratio. The scheme of such a device with all the input and output fields is shown in figure 3, and the relations between them read:

$$\hat{\boldsymbol{o}}' = -\sqrt{R_{\rm BS}}\,\hat{\boldsymbol{b}}^{RE} + \sqrt{T_{\rm BS}}\,\hat{\boldsymbol{b}}^{LN}, \tag{36a}$$

$$\hat{\boldsymbol{d}}' = \sqrt{T_{\rm BS}}\,\hat{\boldsymbol{b}}^{RE} + \sqrt{R_{\rm BS}}\,\hat{\boldsymbol{b}}^{LN}, \tag{36b}$$

$$\hat{\boldsymbol{a}}^{RN} = \sqrt{T_{\rm BS}}\,\hat{\boldsymbol{i}}' + \sqrt{R_{\rm BS}}\,\hat{\boldsymbol{c}}', \tag{36c}$$

$$\hat{\boldsymbol{a}}^{LE} = -\sqrt{R_{\rm BS}}\,\hat{\boldsymbol{i}}' + \sqrt{T_{\rm BS}}\,\hat{\boldsymbol{c}}'. \tag{36d}$$

Optical loss can be included in the above I/O-relations following a standard procedure of complementing the lossless element with two virtual splitters of transmissivity $1 - \epsilon_{\rm BS}$ and reflectivity $\epsilon_{\rm BS}$, with the latter standing for average photon loss due to absorption in the BS (see figure 3 for notations). This allows for additional incoherent vacuum fields associated with the loss to be included in the description as per fluctuation–dissipation theorem [23]. As a result, we get the full I/O-relations for a lossy BS in the following form:

$$\hat{\boldsymbol{o}} = \sqrt{1-\epsilon_{\rm BS}}\left(-\sqrt{R_{\rm BS}}\,\hat{\boldsymbol{b}}^{RE} + \sqrt{T_{\rm BS}}\,\hat{\boldsymbol{b}}^{LN}\right) + \sqrt{\epsilon_{\rm BS}}\,\hat{\boldsymbol{m}}_o, \tag{37a}$$

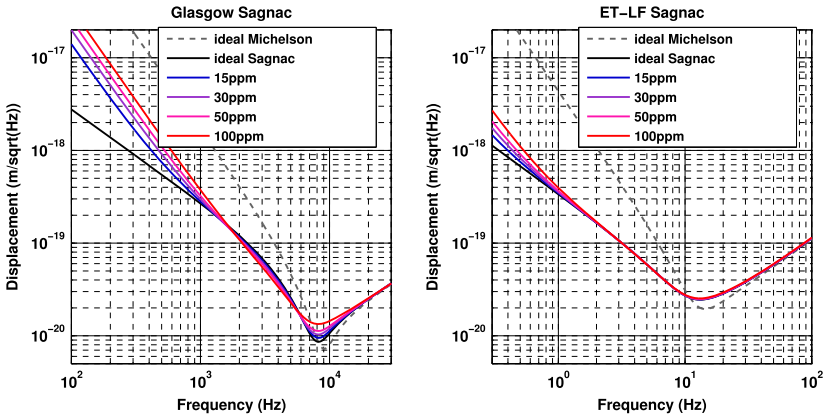

Figure 5. Quantum noise limited sensitivity of the Glasgow Sagnac speed meter proof of concept experiment (left) and a low frequency ET Sagnac interferometer (right) for symmetric losses in the two ring cavities in the arms Ideal Michelson interferometer parameters match those of the corresponding ideal Sagnac interferometer, shown in the same plot.

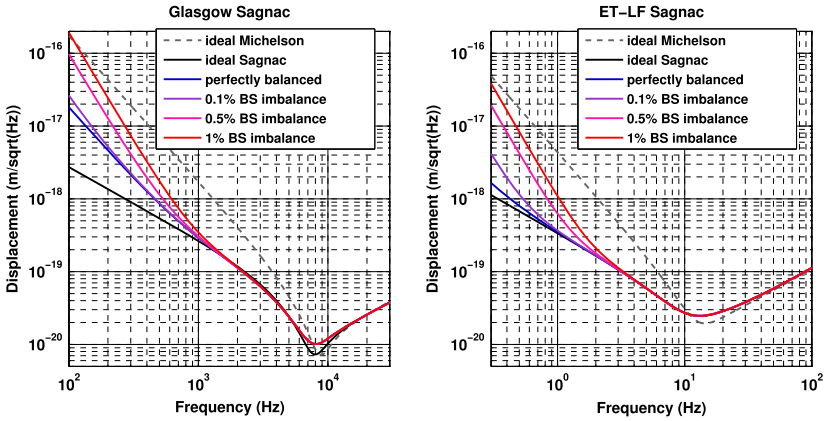

Figure 6. Quantum noise limited sensitivity of the Glasgow Sagnac speed meter proof-of-concept experiment (left) and a low frequency ET Sagnac interferometer (right) for an asymmetric beam splitter. Ideal Michelson interferometer parameters match those of the corresponding ideal Sagnac interferometer, shown in the same plot. (Note that all traces apart from the ones labelled 'ideal', are calculated with symmetric arm cavity losses of 25 ppm.)

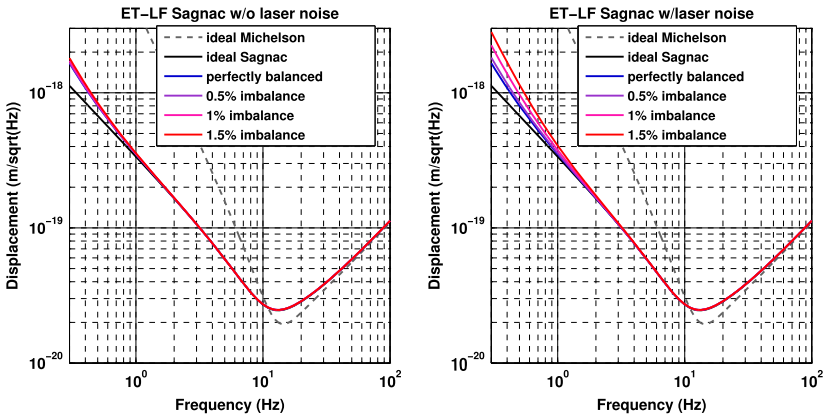

Figure 7. Quantum noise limited sensitivity of the ET Sagnac interferometer in case of asymmetric reflectivities of the ITMs. Left panel shows the influence of this asymmetry when there is no excess laser noise and pump laser is considered ideal. Right panel demonstrates the impact this asymmetry makes in presence of excess laser noise amounting to ten times the vacuum level in power in both, the amplitude and the phase quadratures. Ideal Michelson interferometer parameters match those of the corresponding ideal Sagnac interferometer, shown in the same plot. (Note that all traces apart from the ones labelled 'ideal', are calculated with symmetric arm cavity losses of 25 ppm.)

$$\hat{\boldsymbol{d}} = \sqrt{1-\epsilon_{\rm BS}}\left(\sqrt{T_{\rm BS}}\,\hat{\boldsymbol{b}}^{RE} + \sqrt{R_{\rm BS}}\,\hat{\boldsymbol{b}}^{LN}\right) + \sqrt{\epsilon_{\rm BS}}\,\hat{\boldsymbol{m}}_d, \tag{37b}$$

$$\hat{\boldsymbol{a}}^{RN} = \sqrt{T_{\rm BS}}\left(\sqrt{1-\epsilon_{\rm BS}}\,\hat{\boldsymbol{i}} + \sqrt{\epsilon_{\rm BS}}\,\hat{\boldsymbol{m}}_i\right) + \sqrt{R_{\rm BS}}\left(\sqrt{1-\epsilon_{\rm BS}}\,\hat{\boldsymbol{c}} + \sqrt{\epsilon_{\rm BS}}\,\hat{\boldsymbol{m}}_c\right), \tag{37c}$$

$$\hat{\boldsymbol{a}}^{LE} = -\sqrt{R_{\rm BS}}\left(\sqrt{1-\epsilon_{\rm BS}}\,\hat{\boldsymbol{i}} + \sqrt{\epsilon_{\rm BS}}\,\hat{\boldsymbol{m}}_i\right) + \sqrt{T_{\rm BS}}\left(\sqrt{1-\epsilon_{\rm BS}}\,\hat{\boldsymbol{c}} + \sqrt{\epsilon_{\rm BS}}\,\hat{\boldsymbol{m}}_c\right). \tag{37d}$$

One can check that substitutions $R'_{\rm BS} \to (1-\epsilon_{\rm BS})R_{\rm BS}$ and $T'_{\rm BS} \to (1-\epsilon_{\rm BS})T_{\rm BS}$ lead to a more traditional form of the I/O-relations where $R'_{\rm BS} + T'_{\rm BS} + \epsilon_{\rm BS} = 1$, while the meaning remains unchanged.

Using these relations and the expressions for transfer matrices and response functions of a lossy arm cavity, derived in appendix A, we can calculate I/O-relations for a full Sagnac interferometer in the form:

$$\hat{\boldsymbol{o}} = \mathbb{T}^{i}_{\rm sag}\cdot\hat{\boldsymbol{i}} + \mathbb{T}^{p}_{\rm sag}\cdot\hat{\boldsymbol{p}} + \sum_{\substack{I=L,R\\J=N,E}}\mathbb{N}^{IJ}_{\rm sag}\cdot\hat{\boldsymbol{n}}_{IJ}\sum_{k=i,p}\mathbb{M}^{k}_{\rm sag}\cdot\hat{\boldsymbol{m}}_k + \mathbf{R}^{+}_{\rm sag}x_{+} + \mathbf{R}^{-}_{\rm sag}x_{-}. \tag{38}$$

Using this expression one can finally arrive at the general formula for quantum noise spectral density:

$$S^{x}(\Omega) = \frac{x^2_{\rm SQL}}{\left|\mathbf{H}^{\rm T}_{\zeta}\cdot\mathbf{R}^{-}_{\rm sag}\right|^2}\left\{\mathbf{H}^{\rm T}_{\zeta}\cdot\left[\mathbb{T}^{i}_{\rm sag}\cdot\mathbb{S}^{\rm in}_{i}\cdot\left(\mathbb{T}^{i}_{\rm sag}\right)^{\dagger} + \mathbb{T}^{p}_{\rm sag}\cdot\left(\mathbb{T}^{p}_{\rm sag}\right)^{\dagger}\right]\cdot\mathbf{H}_{\zeta}\right.$$
$$\left. + \sum_{\substack{I=L,R\\J=N,E}}\mathbf{H}^{\rm T}_{\zeta}\cdot\mathbb{N}^{IJ}_{\rm sag}\cdot\left(\mathbb{N}^{IJ}_{\rm sag}\right)^{\dagger}\cdot\mathbf{H}_{\zeta} + \sum_{k=i,p}\mathbf{H}^{\rm T}_{\zeta}\cdot\mathbb{M}^{k}_{\rm sag}\cdot\left(\mathbb{M}^{k}_{\rm sag}\right)^{\dagger}\cdot\mathbf{H}_{\zeta}\right\}. \tag{39}$$

3. Influence on the performance of a small and a large scale speed meter

In this section we present potential applications for the model developed in the previous section. We chose two specific Sagnac speed meter interferometer configurations as examples: the metre-scale experiment currently under construction at Glasgow and a large-scale configuration with parameters suitable for implementation as the low frequency interferometer [25] as part of the planned ET observatory. Both examples are based on Sagnac interferometers employing ring cavities in the arms and a homodyne readout. Neither configuration discussed here contains recycling techniques or squeezed light injection.

Worth noting also is that all the plots presented herein are drawn in assumption that we measure a phase quadrature of the outgoing light. This is by no means an optimal regime for the speed meter in terms of surpassing the SQL (see e.g. section 6.2 of [3]), and much better sub-SQL sensitivity can be achieved with optimally tuned readout phase of Sagnac interferometer. The main goal of this paper is to demonstrate that even with imperfections, the Sagnac interferometer has significant advantage over the Michelson interferometer at low frequencies. To facilitate the reader in getting this message, we placed in all sensitivity plots in this article the sensitivity curves of an ideal (lossless and symmetric) Michelson interferometers with parameters equivalent to the corresponding ideal Sagnac interferometers as a yardstick.

The Glasgow Sagnac speed meter aims to demonstrate the back action reduction of a speed meter compared to a Michelson interferometer with similar parameters. A detailed description of the experimental set up can be found in [19]. The most important parameters of this configuration are listed in the central column of table 1.

The parameters under consideration for the ET low frequency (ET-LF) interferometer were primarily taken from the most recent sensitivity study at the time of writing [10]. Since this design includes power recycling whereas the Glasgow speed meter experiment does not, the input power for ET-LF has been increased from 3.00 to 45.73 W to account for the lack of power recycling cavity gain. This change maintains the intended circulating cavity power of 18 kW. Additionally, to maintain the frequency at which the interferometer is most sensitive, the transmissivity of the cavity input mirrors has been altered from 7000 to 10 000 ppm. This recovers in our model the frequency at which the ET-LF interferometer is intended to be most sensitive. A list of parameters relevant to the model is shown for our ET-LF Sagnac interferometer in the right hand column of table 1.

Figure 5 shows how symmetric losses, i.e. losses that are identical in both ring cavities, degrade the quantum noise limited sensitivity of our two example configurations. The black traces represent perfectly balanced optical configurations with no losses in the interferometer arms. The remaining traces indicate symmetric losses in the range from 15 to 100 ppm[4]. As has been described in the previous section, the main effect of the losses in the arm cavities shows up as an increased level of quantum noise at low frequencies, which features a $1/f^2$ slope. Overall,

[4] In real interferometers, the actual value of round-trip loss depends strongly on the length of the cavities. Longer cavities are known to be more lossy than the shorter ones (see [18, 26]). Here, however, we use the same value for both the short- and the long-base interferometers in order to make a fair comparison between them and make the effect of arm length on the impact of imperfections more profound.

Table 1. Key parameters used to model the quantum-noise limited sensitivity of the Glasgow Sagnac speed meter proof of principle experiment and a large scale ET-LF like Sagnac configuration.

Parameter	Glasgow speed meter	ET speed meter
Power incident on BS	1.7 W	45.73 W
Laser wavelength	1064 nm	1064 nm
Arm cavity round trip length	2.83 m	2×10^4 m
ITM mass	0.85 g	211 kg
ETM mass	100 g	211 kg
ITM transmissivity	700 ppm	10 000 ppm
Photodiode efficiency	95%	95%
Beam splitter loss	1000 ppm	1000 ppm

the loss-driven increase of the quantum noise limited sensitivity is much stronger for the Glasgow speed meter than it is for the ET-LF speed meter. This can be understood by considering the fact that the Glasgow speed meter possesses arm cavity finesse approximately 20 times higher than those of the ET-LF Sagnac configuration. Despite similar round trip loss, the total loss experienced in the short Glasgow speed meter arm cavities is therefore about 20 times higher than for that of the low frequency ET interferometer.

It should be noted that the quantum noise with losses for the short Glasgow speed meter cannot be calculated accurately using the approximation that the arm cavity round trip losses are small compared to the input mirror transmission. Doing so would strongly underestimate the effect of the losses. It is therefore crucial that all quantum noise calculations for the Glasgow speed meter experiment fully account for losses (without relying on approximations), as we have done in the analysis presented in this article.

Figure 6 shows the influence of an imbalance in the reflection to transmission ratio of the main interferometer's BS. Please note that the coloured traces represent configurations with nominal arm cavity losses (i.e. 25 ppm) and different levels of BS imbalance, while for reference the black traces indicate the case of no losses and perfectly balanced transmission and reflection. For a BS imbalance of the order 0.1% we find that the slope of the quantum noise at low frequencies approaches a $1/f^3$ slope, as was discussed and explained earlier in this article.

At first glance it might seem that the ET speed meter tends to be more susceptible to BS imbalance than the Glasgow speed meter (by comparing the separation of the red and dark blue traces). However, in reality this difference only originates from the fact that for a perfectly balanced system the quantum noise of the Glasgow speed meter is already degraded much more from the 25 ppm round trip loss than the quantum noise of the ET interferometer. If we compare the quantum noise with BS imbalance (blue traces) to the case of no losses combined with perfect BS balance (black traces), then the overall quantum noise degradation looks similar for the two example configurations. This can be intuitively understood by considering that a BS imbalance causes a reduction in the cancellation of quantum noise, which is independent of the arm cavity finesse.

Finally, figure 7 illustrates the effect of imbalance of the reflectivities of the two input mirrors combined with the effect of laser noise. Both plots are based on the ET configuration with asymmetric arm cavity input mirror reflectivities. However, the left plot assumes an ideal laser, i.e. the laser output is limited by vacuum noise, while in the right hand plot the presence of excess noise of ten times the vacuum is assumed be present in both quadratures on the laser. As can be seen from this comparison the excess laser noise significantly increases the effect of the imbalances in the interferometer configuration[5].

4. Summary

In this article we have developed for the first time an analytical analysis that can accurately predict the quantum noise limited sensitivity of Sagnac speed meter interferometers featuring arm cavities. In particular, our models do not reply on the common assumption that the arm cavity round trip loss is small compared to the arm cavity input mirror transmission.

We have illustrated the results of our analysis by applying the model to two different speed meter configurations on very different length scales. We find that for the Glasgow speed meter proof-of-concept experiment, symmetric arm cavity losses and BS imbalance have the strongest influence on the achievable quantum noise level, while input mirror imbalances seem to be not too critical. In contrast, we find that for a

[5] The effect shown here is even more profound for a BS imbalance.

10 km long ET Sagnac interferometer the most significant quantum noise degradation is caused by BS imbalances, while symmetric losses and input mirror imbalance play only a minor role.

Acknowledgments

We greatly appreciate all the help and illuminating discussions with A Freise, D Brown, H Miao and S Vyatchanin. We would also like to thank K Strain for his constant support and constructive feedback. The work described in this article is funded by the European Research Council (ERC-2012-StG: 307245). We are grateful for support from Science and Technology Facilities Council (Grant Ref: ST/L000946/1), the Humboldt Foundation, the International Max Planck Partnership (IMPP) and the ASPERA ET-R&D project.

Appendix A. Derivation of input–output relations for imperfect zero-area Sagnac interferometer

In this section, we present a detailed derivation of I/O-relations for an imperfect Sagnac interferometer and derive an unabridged expression for the quantum noise spectral density. We start with the lossy arm cavity relations, then proceed to the imperfect, lossy BS relations and, finally, derive the expressions for output fields of the entire Sagnac interferometer expressed in terms of the input fields.

A.1. Arm cavity input–output relations

The general the I/O-relations of a lossy arm cavity of a Sagnac interferometer can be written as follows

$$\hat{\boldsymbol{b}}^{IJ} = \mathbb{T}^{IJ}_{\rm arm}\cdot\hat{\boldsymbol{a}}^{IJ} + \mathbb{N}^{IJ}_{\rm arm}\cdot\hat{\boldsymbol{n}}^{IJ} + \mathbb{T}^{\bar{I}J}_{\rm arm,r.p.}\cdot\hat{\boldsymbol{a}}^{\bar{I}J} + \mathbb{N}^{\bar{I}J}_{\rm arm,r.p.}\cdot\hat{\boldsymbol{n}}_{\bar{I}J} + \mathbf{R}^{IJ}_{\rm arm}\frac{x_J}{x_{\rm SQL}}. \tag{A.1}$$

To calculate radiation pressure contribution to the transfer matrices as well as to account for effects of cavity detuning on the mirrors' dynamics, we need to calculate the intracavity field as a function of the input fields as well:

$$\hat{\boldsymbol{e}}^{IJ} = \frac{1}{\sqrt{\tau}}\mathbb{L}_J(\Omega)\cdot\left[\sqrt{\gamma^J_{\rm ITM}}\hat{\boldsymbol{a}}^{IJ} + \sqrt{\gamma^J_{\rm loss}}\hat{\boldsymbol{n}}^{IJ}\right] + \frac{1}{2\sqrt{\gamma^J_{\rm ITM}\tau}}\mathbf{R}^{IJ}_{\rm arm}\frac{x_J}{x_{\rm SQL}}, \tag{A.2}$$

where again $J = E, N$ and $\tau = L/c$ is the light travel time between the arm cavity mirrors

$$\mathbb{T}^{IJ}_{\rm arm} = 2\gamma^J_{\rm ITM}\mathbb{L}_J(\Omega) - \mathbb{I} + \mathbb{T}^{IJ}_{\rm r.p.},\ \mathbb{N}^{IJ}_{\rm arm} = 2\sqrt{\gamma^J_{\rm ITM}\gamma^J_{\rm loss}}\mathbb{L}_J(\Omega) + \mathbb{N}^{IJ}_{\rm r.p.}. \tag{A.3}$$

Here

$$\mathbb{L}_J(\Omega) = \frac{1}{\mathcal{D}_J(\Omega)}\begin{bmatrix}\gamma^J_{\rm ITM}+\gamma^J_{\rm loss}-{\rm i}\Omega & -\delta_J\\ \delta_J & \gamma^J_{\rm ITM}+\gamma^J_{\rm loss}-{\rm i}\Omega\end{bmatrix}, \tag{A.4}$$

$$\mathcal{D}_J(\Omega) = \left(\gamma^J_{\rm ITM}+\gamma^J_{\rm loss}-{\rm i}\Omega\right)^2 + \delta_J^2, \tag{A.5}$$

$$\mathbf{R}^{IJ}_{\rm arm}(\Omega) = \sqrt{\frac{16\omega_p P_c^{IJ}\gamma^J_{\rm ITM}}{\mu^J_{\rm arm}\Omega^2 Lc}}\mathbb{L}(\Omega)\cdot\begin{bmatrix}-\sin\Phi_{IJ}\\ \cos\Phi_{IJ}\end{bmatrix} = \sqrt{\frac{4\Theta^{IJ}\gamma^J_{\rm ITM}}{\Omega^2}}\mathbb{L}(\Omega)\cdot\begin{bmatrix}0\\1\end{bmatrix}. \tag{A.6}$$

In the equantions above Φ_{IJ} stands for phases, the IJ-beam field has at the ITM of the Jth arm cavity. Its choice is arbitrary and depends on the chosen carrier field reference phase, so we can always set it to zero, as it is done in the second equation. $\Theta^{IJ} = 4\omega_p P_c^{IJ}/(\mu^J_{\rm arm}cL)$ is the normalized power circulating in the Ith arm in the Jth beam, $\mu^J_{\rm arm} = 2M^J_{\rm ITM}M^J_{\rm ETM}/(M^J_{\rm ITM}+2M^J_{\rm ETM})$ is an effective mass of the Jth arm with $M^J_{\rm ITM}$ and $2M^J_{\rm ETM}$ being the masses of ITM and ETM (note that there are two of them in each cavity), $\delta_J = \omega_J - \omega_p$ is the Jth cavity resonance frequency, ω_J, detuning from the pump laser frequency ω_p, and the cavity half-bandwidths due to ITM power transmissivity, $T^J_{\rm ITM}$, and due to loss, $T^J_{\rm loss}$, read

$$\gamma^J_{\rm ITM} = \frac{cT^J_{\rm ITM}}{4L},\quad \gamma^J_{\rm loss} = \frac{cT^J_{\rm loss}}{4L}. \tag{A.7}$$

To calculate the radiation pressure contribution we need to know how the mirrors move under the radiation pressure force from both beams. Writing down the equations of motion for each mirror and then combining them in the effective arm degree of freedom x_J, one can get the following expression for the latter in the frequency domain:

$$x_J = x_J^{\rm signal} + \hat{x}_J^{r.p.} = x_J^{\rm signal} + \chi^J(\Omega)\left[\hat{F}^{IJ} + \hat{F}^{\bar{I}J}\right], \text{ where } \chi^J(\Omega) = -\frac{1}{\mu^J_{\rm arm}\Omega^2}, \tag{A.8}$$

where we assumed the dynamics of the arm to be that of a free mass with an effective mass $\mu^J_{\rm arm}$. In principle, it is always possible to introduce more complicated dynamics into our model by changing the shape of the mechanical susceptibility functions $\chi^J(\Omega)$. The radiation pressure forces created by each beam read:

$$\begin{aligned}\hat{F}^{IJ} &= 2\frac{\hbar\omega_p}{c}\left(\mathbf{E}^{IJ}\right)^{\rm T}\cdot\hat{\boldsymbol{e}}_{IJ} = \sqrt{\frac{8\hbar\omega_p P_c^{IJ}}{c^2}}\begin{bmatrix}1\\0\end{bmatrix}^{\rm T}\cdot\hat{\boldsymbol{e}}_{IJ} = \hat{F}^{IJ}_{\rm r.p.} - K^{IJ}_{\rm arm}(\Omega)x_J \\ &= \sqrt{2\hbar\mu^J_{\rm arm}\Theta^{IJ}}\begin{bmatrix}1\\0\end{bmatrix}^{\rm T}\cdot\mathbb{L}_J(\Omega)\cdot\left[\sqrt{\gamma^J_{\rm ITM}}\hat{\boldsymbol{a}}^{IJ} + \sqrt{\gamma^J_{\rm loss}}\hat{\boldsymbol{n}}^{IJ}\right] - \frac{\mu^J_{\rm arm}\Theta^{IJ}\delta^J}{\mathcal{D}_J(\Omega)}x_J.\end{aligned} \tag{A.9}$$

Here the first term, $\hat{F}^{IJ}_{\rm r.p.}$, is the pure fluctuational force, and the last term, $K^{IJ}_{\rm arm}(\Omega)x_J$, is the dynamical back-action term with $K^{IJ}_{\rm arm}(\Omega)$ an optical rigidity, which is only relevant for non-zero arm detuning δ^J.

Then we substitute the expression (A.9) into (A.8) and get the new equation for the cavity mirrors dynamics:

$$x_J = x_J^{\rm signal} + \chi^J(\Omega)\left[\hat{F}^{IJ}_{\rm r.p.} + \hat{F}^{\bar{I}J}_{\rm rp} - \left(K^{IJ}_{\rm arm} + K^{\bar{I}J}_{\rm arm}\right)x_J\right],$$

which can be resolved in x_J to give:

$$x_J = x_J^{\rm signal} + \chi^J_{\rm new}(\Omega)\left[\hat{F}^{IJ}_{\rm r.p.} + \hat{F}^{\bar{I}J}_{\rm rp}\right], \tag{A.10}$$

where the new modified mechanical susceptibility reads:

$$\chi^J_{\rm new}(\Omega) = \frac{\chi^J(\Omega)}{1 + \chi^J(\Omega)\left(K^{IJ}_{\rm arm}(\Omega) + K^{\bar{I}J}_{\rm arm}(\Omega)\right)}. \tag{A.11}$$

Note that for cavities tuned to resonance, $\chi^J_{\rm new}(\Omega) = \chi^J(\Omega)$.

The expressions for $\mathbb{T}^{IJ}_{\rm r.p.}$ and $\mathbb{N}^{IJ}_{\rm r.p.}$ are obtained by substituting (A.10) into the following formula, representing the back-action induced contribution to the output field:

$$\Delta\hat{\boldsymbol{b}}^{IJ}_{\rm r.p.} = \mathbf{R}^{IJ}_{\rm arm}\frac{x_J - x_J^{\rm signal}}{x_{\rm SQL}}, \tag{A.12}$$

and collecting the coefficients in front of the corresponding light field. Thereby we arrive at the following expressions:

$$\mathbb{T}^{IJ}_{\rm r.p.} = 2\mu^J_{\rm arm}\chi^J_{\rm new}\Theta^{IJ}\gamma^J_{\rm ITM}\mathbb{L}_J(\Omega)\cdot\begin{bmatrix}0&0\\1&0\end{bmatrix}\cdot\mathbb{L}_J(\Omega), \tag{A.13}$$

$$\mathbb{N}^{IJ}_{\rm r.p.} = 2\mu^J_{\rm arm}\chi^J_{\rm new}\Theta^{IJ}\sqrt{\gamma^J_{\rm ITM}\gamma^J_{\rm loss}}\mathbb{L}_J(\Omega)\cdot\begin{bmatrix}0&0\\1&0\end{bmatrix}\cdot\mathbb{L}_J(\Omega). \tag{A.14}$$

The two fields leaving the interferometer and mixing at the BS are $\hat{\boldsymbol{b}}^{LN}$ and $\hat{\boldsymbol{b}}^{RE}$. They can be expressed in terms of the input fields, $\hat{\boldsymbol{a}}^{RN}$ and $\hat{\boldsymbol{a}}^{LE}$, as well as of noise fields $\hat{\boldsymbol{n}}^{IJ}$ using continuity conditions:

$$\hat{\boldsymbol{a}}^{LN} = \hat{\boldsymbol{b}}^{LE}, \quad \hat{\boldsymbol{a}}^{RE} = \hat{\boldsymbol{b}}^{RN}. \tag{A.15}$$

Then the general expression for each arm's I/O-relations read:

$$\hat{\boldsymbol{b}}^{LN} = \mathbb{T}^{LN}_{\rm arm}\left[\left(\mathbb{I} - \mathbb{T}^{RE}_{\rm r.p.}\mathbb{T}^{LN}_{\rm r.p.}\right)^{-1}\mathbb{T}^{RE}_{\rm r.p.}\hat{\boldsymbol{f}}^{RN} + \left(\mathbb{I} - \mathbb{T}^{RE}_{\rm r.p.}\mathbb{T}^{LN}_{\rm r.p.}\right)^{-1}\hat{\boldsymbol{f}}^{LE}\right] + \hat{\boldsymbol{f}}^{LN}, \tag{A.16a}$$

$$\hat{\boldsymbol{b}}^{RE} = \mathbb{T}^{RE}_{\rm arm}\left[\left(\mathbb{I} - \mathbb{T}^{LN}_{\rm r.p.}\mathbb{T}^{RE}_{\rm r.p.}\right)^{-1}\hat{\boldsymbol{f}}^{RN} + \left(\mathbb{I} - \mathbb{T}^{LN}_{\rm r.p.}\mathbb{T}^{RE}_{\rm r.p.}\right)^{-1}\mathbb{T}^{LN}_{\rm r.p.}\hat{\boldsymbol{f}}^{LE}\right] + \hat{\boldsymbol{f}}^{RE}, \tag{A.16b}$$

where

$$\hat{\boldsymbol{f}}^{LN} = \mathbb{T}^{RN}_{\rm r.p.}\hat{\boldsymbol{a}}^{RN} + \mathbb{N}^{LN}_{\rm arm}\hat{\boldsymbol{n}}^{LN} + \mathbb{N}^{RN}_{\rm r.p.}\hat{\boldsymbol{n}}^{RN} + \mathbf{R}^{LN}_{\rm arm}\frac{x_N}{x_{\rm SQL}}, \tag{A.16c}$$

$$\hat{\boldsymbol{f}}^{RN} = \mathbb{T}^{RN}_{\rm arm}\hat{\boldsymbol{a}}^{RN} + \mathbb{N}^{RN}_{\rm arm}\hat{\boldsymbol{n}}^{RN} + \mathbb{N}^{LN}_{\rm r.p.}\hat{\boldsymbol{n}}^{LN} + \mathbf{R}^{RN}_{\rm arm}\frac{x_N}{x_{\rm SQL}}, \tag{A.16d}$$

$$\hat{\boldsymbol{f}}^{LE} = \mathbb{T}^{LE}_{\rm arm}\hat{\boldsymbol{a}}^{LE} + \mathbb{N}^{LE}_{\rm arm}\hat{\boldsymbol{n}}^{LE} + \mathbb{N}^{RE}_{\rm r.p.}\hat{\boldsymbol{n}}^{RE} + \mathbf{R}^{LE}_{\rm arm}\frac{x_E}{x_{\rm SQL}}, \tag{A.16e}$$

$$\hat{\boldsymbol{f}}^{RE} = \mathbb{T}^{LE}_{\text{r.p.}}\hat{\boldsymbol{a}}^{LE} + \mathbb{N}^{RE}_{\text{arm}}\hat{\boldsymbol{n}}^{RE} + \mathbb{N}^{LE}_{\text{r.p.}}\hat{\boldsymbol{n}}^{LE} + \mathbf{R}^{RE}_{\text{arm}}\frac{x_E}{x_{\text{SQL}}}. \tag{A.16f}$$

A.1.1. Special case of resonant arms. These bulky relations become significantly simpler as the arm cavities are set to resonance, i.e. for $\delta^J = 0$. Then the radiation pressure matrices defined in (A.13) and (A.14) take the much simpler form:

$$\mathbb{T}^{IJ}_{\text{r.p.}} = \mathrm{e}^{2\mathrm{i}\beta^J_{\text{arm}}}\begin{bmatrix} 0 & 0 \\ -\mathcal{K}^{IJ}_{\text{arm}} & 0 \end{bmatrix}, \quad \mathbb{N}^{IJ}_{\text{r.p.}} = \sqrt{\frac{\gamma^J_{\text{loss}}}{\gamma^J_{\text{ITM}}}}\,\mathbb{T}^{IJ}_{\text{r.p.}}, \quad \mathbf{R}^{IJ}_{\text{arm}} = \sqrt{2\mathcal{K}^{IJ}_{\text{arm}}}\,\mathrm{e}^{\mathrm{i}\beta^J_{\text{arm}}}\begin{bmatrix} 0 \\ 1 \end{bmatrix}, \tag{A.17}$$

where optomechanical coupling factor of a lossy arm is defined as:

$$\mathcal{K}^{IJ}_{\text{arm}} = \frac{\Theta^{IJ}\gamma^J_{\text{ITM}}}{\Omega^2\left[\left(\gamma^J_{\text{ITM}} + \gamma^J_{\text{loss}}\right)^2 + \Omega^2\right]}, \quad \beta^J_{\text{arm}} = \arctan\frac{\Omega}{\gamma^J_{\text{ITM}} + \gamma^J_{\text{loss}}}. \tag{A.18}$$

In this particular case, the radiation pressure matrices $\mathbb{T}^{IJ}_{\text{r.p.}}$ and $\mathbb{N}^{IJ}_{\text{r.p.}}$ are orthogonal to each other, meaning that any product of them, irrespective of what value the indices I, J have, is zero. Transfer matrices (A.3) become:

$$\mathbb{T}^{IJ}_{\text{arm}} = \mathrm{e}^{2\mathrm{i}\beta^J_{\text{arm}}}\begin{bmatrix} \mathcal{T}^J_{\text{arm}} & 0 \\ -\mathcal{K}^{IJ}_{\text{arm}} & \mathcal{T}^J_{\text{arm}} \end{bmatrix}, \quad \mathbb{N}^{IJ}_{\text{arm}} = \sqrt{\frac{\gamma^J_{\text{loss}}}{\gamma^J_{\text{ITM}}}}\,\mathrm{e}^{2\mathrm{i}\beta^J_{\text{arm}}}\begin{bmatrix} \mathcal{N}^J_{\text{arm}} & 0 \\ -\mathcal{K}^{IJ}_{\text{arm}} & \mathcal{N}^J_{\text{arm}} \end{bmatrix}, \tag{A.19}$$

where

$$\mathcal{T}^J_{\text{arm}}(\Omega) = \frac{\gamma^J_{\text{ITM}} - \gamma^J_{\text{loss}} + \mathrm{i}\Omega}{\gamma^J_{\text{ITM}} + \gamma^J_{\text{loss}} + \mathrm{i}\Omega}, \quad \mathcal{N}^J_{\text{arm}}(\Omega) = \frac{2\gamma^J_{\text{ITM}}}{\gamma^J_{\text{ITM}} + \gamma^J_{\text{loss}} + \mathrm{i}\Omega}.$$

This simplifies the I/O-relations (A.16) substantially:

$$\hat{\boldsymbol{b}}^{LN} = \mathbb{T}^{LN}_{\text{arm}}\left[\mathbb{T}^{RE}_{\text{r.p.}}\hat{\boldsymbol{f}}^{RN} + \hat{\boldsymbol{f}}^{LE}\right] + \hat{\boldsymbol{f}}^{LN}, \tag{A.20a}$$

$$\hat{\boldsymbol{b}}^{RE} = \mathbb{T}^{RE}_{\text{arm}}\left[\hat{\boldsymbol{f}}^{RN} + \mathbb{T}^{LN}_{\text{r.p.}}\hat{\boldsymbol{f}}^{LE}\right] + \hat{\boldsymbol{f}}^{RE}. \tag{A.20b}$$

These simplified expressions can be used to estimate the influence of different asymmetries on the Sagnac interferometer sensitivity. To make the final step in the calculation of the spectral density, we need to refer to the BS relations, which is presented in the next subsection:

A.2. BS input/output relations

The input and output fields of the BS are shown in figure 3. The corresponding input–output relations read:

$$\hat{\boldsymbol{o}} = \sqrt{1-\epsilon_{\text{BS}}}\left(-\sqrt{R_{\text{BS}}}\hat{\boldsymbol{b}}^{RE} + \sqrt{T_{\text{BS}}}\hat{\boldsymbol{b}}^{LN}\right) + \sqrt{\epsilon_{\text{BS}}}\hat{\boldsymbol{m}}_o, \tag{A.21a}$$

$$\hat{\boldsymbol{q}} = \sqrt{1-\epsilon_{\text{BS}}}\left(\sqrt{T_{\text{BS}}}\hat{\boldsymbol{b}}^{RE} + \sqrt{R_{\text{BS}}}\hat{\boldsymbol{b}}^{LN}\right) + \sqrt{\epsilon_{\text{BS}}}\hat{\boldsymbol{m}}_p, \tag{A.21b}$$

$$\hat{\boldsymbol{a}}^{RN} = \sqrt{T_{\text{BS}}}\left(\sqrt{1-\epsilon_{\text{BS}}}\hat{\boldsymbol{i}} + \sqrt{\epsilon_{\text{BS}}}\hat{\boldsymbol{m}}_i\right) + \sqrt{R_{\text{BS}}}\left(\sqrt{1-\epsilon_{\text{BS}}}\hat{\boldsymbol{p}} + \sqrt{\epsilon_{\text{BS}}}\hat{\boldsymbol{m}}_p\right), \tag{A.21c}$$

$$\hat{\boldsymbol{a}}^{LE} = -\sqrt{R_{\text{BS}}}\left(\sqrt{1-\epsilon_{\text{BS}}}\hat{\boldsymbol{i}} + \sqrt{\epsilon_{\text{BS}}}\hat{\boldsymbol{m}}_i\right) + \sqrt{T_{\text{BS}}}\left(\sqrt{1-\epsilon_{\text{BS}}}\hat{\boldsymbol{p}} + \sqrt{\epsilon_{\text{BS}}}\hat{\boldsymbol{m}}_p\right). \tag{A.21d}$$

We introduced a BS asymmetry offset, $\alpha_{\text{BS}} \ll 1$, in equation (27). Losses at the BS are accounted for by introducing the loss factor $\epsilon_{\text{BS}} \ll 1$ and corresponding vacuum fields, $\hat{\boldsymbol{m}}_{i,p}$. Substituting equations (A.21c), (A.21d) into equations (A.16a), (A.16b) and substituting the result into equation (A.21a), we finally get the full interferometer I/O relations:

$$\hat{\boldsymbol{o}} = \mathbb{T}^i_{\text{sag}}\cdot\hat{\boldsymbol{i}} + \mathbb{T}^p_{\text{sag}}\cdot\hat{\boldsymbol{p}} + \sum_{\substack{I=L,R\\J=N,E}}\mathbb{N}^{IJ}_{\text{sag}}\cdot\hat{\boldsymbol{n}}_{IJ}\sum_{k=i,p}\mathbb{M}^k_{\text{sag}}\cdot\hat{\boldsymbol{m}}_k + \mathbf{R}^+_{\text{sag}}x_+ + \mathbf{R}^-_{\text{sag}}x_-. \tag{A.22}$$

Here $\mathbb{M}^{i,p}_{\text{sag}}$ stand for transfer matrices for additional noise associated with the BS loss.

Collecting the terms in front of corresponding vacuum fields and mechanical displacement terms, one can get the unabridged expressions for transfer matrices and represent the I/O relations. These expressions are rather cumbersome and opaque, though straightforward to derive, so we omit them here. The quantum noise power spectral density can be then calculated using the general rule (14), which yields:

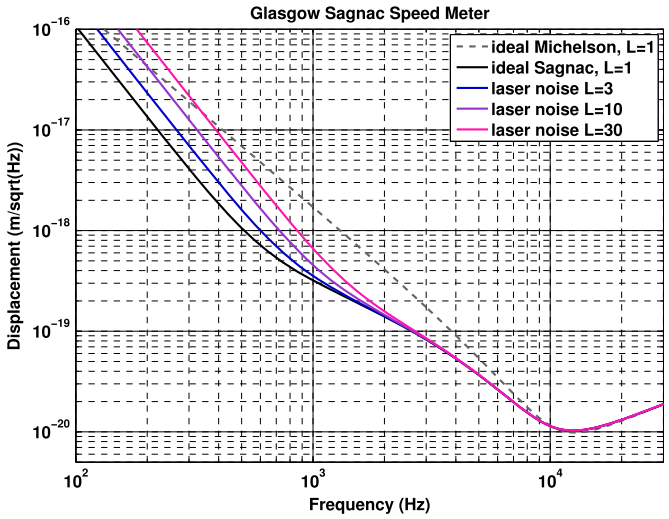

Figure B1. Spectral density plots for a table-top Sagnac interferometer with parameters given in table 1. The influence of laser noise in the presence of 1% asymmetry of the beam splitter for different levels of laser noise. We assume fluctuations of two quadratures of laser light independent and having the same spectral density L which takes the values $L = 1,\ 3,\ 10,\ 30$ times the vacuum level. Ideal Michelson interferometer parameters match those of the corresponding ideal Sagnac interferometer, shown in the same plot.

$$S^x(\Omega) = \frac{x_{\rm SQL}^2}{\left|\mathbf{H}_\zeta^{\rm T}\cdot\mathbf{R}_{\rm sag}^-\right|^2}\left\{\mathbf{H}_\zeta^{\rm T}\cdot\left[\mathbb{T}_{\rm sag}^i\cdot\mathbb{S}_i^{\rm in}\cdot\left(\mathbb{T}_{\rm sag}^i\right)^\dagger + \mathbb{T}_{\rm sag}^p\cdot\left(\mathbb{T}_{\rm sag}^p\right)^\dagger\right]\cdot\mathbf{H}_\zeta + \sum_{\substack{I=L,R\\J=N,E}}\mathbf{H}_\zeta^{\rm T}\cdot\mathbb{N}_{\rm sag}^{IJ}\cdot\left(\mathbb{N}_{\rm sag}^{IJ}\right)^\dagger\cdot\mathbf{H}_\zeta + \sum_{k=i,p}\mathbf{H}_\zeta^{\rm T}\cdot\mathbb{M}_{\rm sag}^k\cdot\left(\mathbb{M}_{\rm sag}^k\right)^\dagger\cdot\mathbf{H}_\zeta\right\}. \tag{A.23}$$

Here we normalized quantum noise to the dARM signal, as indicated by the denominator, where $\mathbf{R}_{\rm sag}^-$ stands for the interferometer response function to differential motion of the mirrors.

Appendix B. Laser noise in asymmetric Sagnac interferometer

The main implication an asymmetry of the interferometer has in regards to the quantum noise is the leakage of laser noise to the output port. Our approach allows to account for this effect assuming a simple model of laser noise as an excess fluctuation on top of the quantum uncertainties of the input laser light. If we assume that the amplitude and phase fluctuations of the carrier light are uncorrelated and characterized by spectral densities $L_c > 1$ and $L_s > 1$, respectively, then the input state of the common mode light field $\hat{\boldsymbol{p}}$ reads:

$$\mathbb{S}_p^{\rm in} = \begin{bmatrix} L_c & 0 \\ 0 & L_s \end{bmatrix}, \tag{B.1}$$

and the general quantum noise spectral density formula (A.23) shall be slightly modified to:

$$S^x(\Omega) = \frac{x_{\rm SQL}^2}{\left|\mathbf{H}_\zeta^{\rm T}\cdot\mathbf{R}_{\rm sag}^-\right|^2}\left\{\mathbf{H}_\zeta^{\rm T}\cdot\left[\mathbb{T}_{\rm sag}^i\cdot\mathbb{S}_i^{\rm in}\cdot\left(\mathbb{T}_{\rm sag}^i\right)^\dagger + \mathbb{T}_{\rm sag}^p\cdot\mathbb{S}_p^{\rm in}\cdot\left(\mathbb{T}_{\rm sag}^p\right)^\dagger\right]\cdot\mathbf{H}_\zeta + \sum_{\substack{I=L,R\\J=N,E}}\mathbf{H}_\zeta^{\rm T}\cdot\mathbb{N}_{\rm sag}^{IJ}\cdot\left(\mathbb{N}_{\rm sag}^{IJ}\right)^\dagger\cdot\mathbf{H}_\zeta + \sum_{k=i,p}\mathbf{H}_\zeta^{\rm T}\cdot\mathbb{M}_{\rm sag}^k\cdot\left(\mathbb{M}_{\rm sag}^k\right)^\dagger\cdot\mathbf{H}_\zeta\right\}. \tag{B.2}$$

The effect that such laser noise has on the quantum noise sensitivity is shown in figure B1 . The chosen span of L values starts at the shot noise level of $L = 1$, which for the 1.7 W laser to be used in the Glasgow prototype Sagnac interferometer corresponds to the relative intensity noise (RIN) ASD of 4.7×10^{-10} Hz$^{-1/2}$. The upper value of $L = 30$ corresponds to the level of RIN available for the same 1.7 W laser with reasonable intensity pre-stabilization, i.e. to the RIN ASD of $\sim 1.4 \times 10^{-8}$ Hz$^{-1/2}$.

References

[1] Harry G M and (The LIGO Scientific Collaboration) 2010 *Class. Quantum Grav.* **27** 084006
[2] Braginsky V B and Khalili F J 1990 *Phys. Lett.* A **147** 251–6
[3] Danilishin S L and Khalili F Y 2012 *Living Rev. Relativ.* **15** 5
[4] Braginsky V B, Gorodetsky M L, Khalili F Y and Thorne K S 2000 *Phys. Rev.* D **61** 044002
[5] Purdue P 2002 *Phys. Rev.* D **66** 022001
[6] Purdue P and Chen Y 2002 *Phys. Rev.* D **66** 122004
[7] Chen Y 2003 *Phys. Rev.* D **67** 122004
[8] Danilishin S L 2004 *Phys. Rev.* D **69** 102003
[9] Punturo M *et al* 2010 *Class. Quantum Grav.* **27** 084007
[10] Hild S *et al* 2011 *Class. Quantum Grav.* **28** 094013
[11] Müller-Ebhardt H 2008 On quantum effects in the dynamics of macroscopic test masses *PhD Thesis* University of Hannover (http://edok01.tib.uni-hannover.de/edoks/e01dh09/58958698X.pdf)
[12] Müller-Ebhardt H, Rehbein H, Hild S, Freise A, Chen Y, Schnabel R, Danzmann K and Lück H 2009 Review of quantum non-demolition schemes for the Einstein Telescope *ET Technical Note* ET-010-09
[13] Chen Y, Danilishin S, Khalili F and Müller-Ebhardt H 2011 *Gen. Relativ. Gravit.* **43** 671–94
[14] Ward R L *et al* 2008 *Class. Quantum Grav.* **25** 114030
[15] Hild S *et al* 2009 *Class. Quantum Grav.* **26** 055012
[16] Wang M, Bond C, Brown D, Brückner F, Carbone L, Palmer R and Freise A 2013 *Phys. Rev.* D **87** 096008
[17] Barr B *et al* 2012 Ligo 3 strawman design, team red *Technical Report* (Washington, DC: LIGO Scientific Collaboration) (https://dcc.ligo.org/public/0086/T1200046/001/LIGO-T1200042-v1.pdf)
[18] Miao H, Yang H, Adhikari R X and Chen Y 2014 *Class. Quantum Grav.* **31** 165010
[19] Gräf C *et al* 2014 *Class. Quantum Grav.* **31** 215009
[20] Braginsky V B, Gorodetsky M L, Khalili F Y, Matsko A B, Thorne K S and Vyatchanin S P 2003 *Phys. Rev.* D **67** 082001
[21] Caves C and Schumaker B 1985 *Phys. Rev.* A **31** 3068–92
[22] Caves C and Schumaker B 1985 *Phys. Rev.* A **31** 3093–111
[23] Callen H and Welton T 1951 *Phys. Rev.* **83** 34–40
[24] Kimble H, Levin Y, Matsko A, Thorne K and Vyatchanin S 2002 *Phys. Rev.* D **65** 022002
[25] Hild S, Chelkowski S, Freise A, Franc J, Morgado N, Flaminio R and DeSalvo R 2010 *Class. Quantum Grav.* **27** 015003
[26] Evans M, Barsotti L, Kwee P, Harms J and Miao H 2013 *Phys. Rev.* D **88** 022002